Progress In Electromagnetics Research, Vol. 146, 167–180, 2014

Efficiency Improvement of *p-i-n* Solar Cell by Embedding Quantum Dots

Yi-Hsien Lin and Jean-Fu Kiang*

Abstract—A model of solar cell embedding quantum dots in the intrinsic layer of a *p-i-n* solar cell has been presented. With proper selection of material, size and fractional volume, quantum dots can provide an intermediate band between the valence and conduction bands of the matrix material, which will absorb photons with energy lower than the original bandgap to absorb more incident photons in the otherwise unused spectral irradiance. The design approach to acquire the highest efficiency of the conventional *p-i-n* solar cell is presented as a benchmark. Quantum dots are then embedded in the intrinsic region of the reference solar cell to improve its efficiency. InAs is chosen to implement the quantum dots, to be embedded in the *p-i-n* solar cell made of GaAs. With a more packed arrangement of QD's from that in the literatures, the simulation results shows that the efficiency of the conventional GaAs *p-i-n* solar cell can be increased by 1.05%.

1. INTRODUCTION

In conventional solar cells, the photons from solar radiation are collected in the *p-n* junctions [1]. Their efficiency is constrained by the Shockley-Queisser limit [2], due to blackbody radiation [3], spectral loss, excessive energy of the absorbed photons, and recombination loss [4]. Up to August 2013, the highest efficiency achieved by a single-layer solar cell, made of GaAs, is 28.8% [5, 6].

Multi-junction solar cells [7, 8] and light-concentrated solar cells [9] have been proposed to break the efficiency limit. The efficiency has been pushed to 37.9% with a three-layered solar cell, composed of InGaP/GaAs/InGaAs [6], and 44.4%, under 302 suns of concentration [6].

The intermediate-band solar cells (IBSC), has also been proposed to increase the efficiency. These solar cells involve a two-step transition: A photon with energy higher than the bandgap between the valence and the intermediate bands is absorbed to generate an electron. Then, another photon with energy higher than the bandgap between the intermediate and the conduction bands pumps the previous electron to the conduction band [10]. By providing an additional intermediate band between the valence and the conduction bands, photon absorption has been made more efficient [7]. QD solar cell is one of the methods to implement IBSC's. The quantum dots are embedded in a matrix to form an intermediate band, with its energy level dependent on the QD size. An alternative form of IBSC is the bulk IB solar cells, in which the intermediate bands are created with strongly mismatched alloys [11] or high concentration of impurities such as rare-earth elements [7] to create multiple intermediate bands.

There are at least two types of process to implement quantum dots. The first one makes colloidal QD's, using materials like CdSe and PbS. The colloidal QD's have been implemented in various sizes and shapes, as well as integrated with conductive polymers.

The second type is called epitaxial QD's, which are self-assembled nano-crystallites, grown with molecular beam epitaxy (MBE) or metal organic chemical vapor deposition (MOCVD) process in the

Received 27 March 2014, Accepted 16 May 2014, Scheduled 26 May 2014

* Corresponding author: Jean-Fu Kiang (jfkiang@ntu.edu.tw).

The authors are with the Department of Electrical Engineering, Graduate Institute of Communication Engineering, National Taiwan University, Taipei, Taiwan.

Stranski-Krastanov growth mode [12, 13]. They can be grown at regular spacings in the intrinsic layer of a *p-i-n* solar cell. The Fermi-Dirac distribution of the intermediate band is made 1/2 by inserting an *n*-type δ-doped layers between two adjacent layers of QD's, with the same doping density per area as the QD's, in order to have the same number of states in the intermediate band to accommodate electrons coming up from the valence band with that to supply electrons to be pumped into the conduction band [14]. The size of quantum dots also affects the absorption and recombination properties of the semiconductor material [15], which will be considered in designing the intermediate band.

Quantum-dot solar cells have been claimed to improve the efficiency over the conventional solar cells. However, it has been found that when QD's made of InAs are embedded in a GaAs solar cell, the efficiency is reduced [10, 16]. If the additional recombination current attributed to embedding the QD's dominates over the additional generation current, a lower efficiency than the conventional solar cell is achieved. In this work, the arrangement of QD's in the intrinsic region as in [10, 16–19] is made more packed to increase the maximum available fractional volume of QD's. By increasing the fractional volume, the generation process is made stronger than the recombination process so that the efficiency of the GaAs solar cell can be increased.

In this work, InAs quantum dots are analyzed and designed to increase the efficiency of the conventional *p-i-n* solar cells made of GaAs. The basic theories are briefly reviewed in Section 2, simulation results and discussions are presented in Section 3, and some conclusions are drawn in Section 4.

2. REVIEW OF BASIC THEORIES

2.1. Energy Level of Spherical Quantum Dots

The QD's can be grown in pyramidal shape by self-assembling in the Stransky-Kastranov mode [12]. The size of QD's is much smaller than the working wavelength, and their shape can be approximated as an ideal sphere [20] in deriving the relation between its size and the effective band-gap, using the effective mass approximation [20].

By solving the Schrodinger equation for a spherical particle of radius a, a dispersion relation can be derived as [21]

$$\beta a \cot \beta a = -\frac{m^*}{m_o}(\alpha a + 1) = 1 - \frac{m^*}{m_o} - \sqrt{\left(\frac{m^*}{m_o}\right)\left(\frac{2m^* V_o a^2}{\hbar^2} - \beta^2 a^2\right)} \tag{1}$$

where m^* and m_o are the effective mass of an electron (or a hole) in and outside the well, respectively [22]; $\hbar$ is the reduced Plank's constant, and V_o is the confining potential. The energy level, E, is related to the eigenvalue, β, as

$$E = \frac{\hbar^2 \beta^2}{2m^*} \tag{2}$$

Figure 1 shows the band diagram of a quantum dot immersed in a semiconductor matrix. The effective bandgap of a QD, immersed in the matrix, becomes

$$E_g^{\mathrm{QD}} = E_g^{\mathrm{bulk}} + \Delta E_g \tag{3}$$

with

$$\Delta E_g = \Delta E_e + \Delta E_h \tag{4}$$

where

$$\Delta E_e = \frac{\hbar^2 \beta_e^2}{2m_e^*}, \qquad \Delta E_h = \frac{\hbar^2 \beta_h^2}{2m_h^*} \tag{5}$$

m_e^* and m_h^* are the effective mass of an electron and a light hole, respectively. Both light hole and heavy hole states exist in InAs. Compared with the heavy hole, a light hole has a lower m_h^*, leading to a wider bandgap shift based on (5). β_e and β_h are derived from the dispersion relation in (1), where $V_{oe} = V_{oh} = V_o = (E_g^{\mathrm{mat}} - E_g^{\mathrm{bulk}})/2$. As mentioned in [23], any combination of V_{oe} and V_{oh} can reach a similar solution as long as $V_{oe} + V_{oh}$ is the same. Relevant parameters for the calculations in (5) are listed in Table 1.

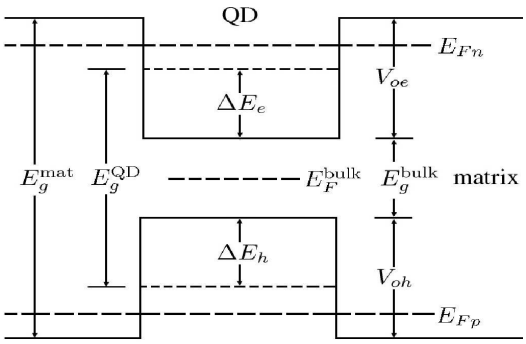

Figure 1. Band diagram of a quantum dot immersed in a semiconductor matrix; E_g^{mat} and E_g^{bulk} are the bandgaps of the matrix and the bulk material of QD's, respectively; V_{oe} and V_{oh} are the confining potential of electrons and holes, respectively; E_g^{QD} is the effective bandgap of a QD; E_F^{bulk} is the Fermi level in the bulk material of QD's; E_{Fn} and E_{Fp} are the Fermi levels of electrons and holes, respectively, in the matrix.

Table 1. Parameters for the calculation of InAs QD's in GaAs matrix [21, 24, 25].

E_g^{mat}	E_g^{bulk}	m_e^*/m_e	m_h^*/m_e
1.42 eV	0.36 eV	0.028	0.33

m_e: mass of a free electron.

2.2. Materials Embedding Quantum Dots

If the size of QD's is much smaller than the light wavelength in the matrix [26], the dielectric properties of the QD's can be estimated using the dipole approximation. Consider a time-harmonic external field, $\bar{E}(t) = \hat{E}E(\omega)\cos(\omega t)$, the polarization density of QD's can be expressed as $P(\omega) = N\langle\bar{p}(\omega)\rangle = \epsilon_0\chi(\omega)E(\omega)$ [27], where N is the number density. The susceptability can be expressed as

$$\chi(\omega) = \frac{N}{\epsilon_0\hbar}\sum_{nm}(\rho_{mm} - \rho_{nn})\left(\frac{p_{mn}p_{nm}}{\omega_{nm} - \omega_0 + j\gamma_{nm}} + \frac{p_{mn}p_{nm}}{\omega_{nm} + \omega_0 - j\gamma_{nm}}\right) \tag{6}$$

where $\omega_{nm} = (E_n - E_m)/\hbar$, E_n and E_m are the energy levels of eigenstates n and m, respectively; γ_{nm} is the HWHM (half-width at half-maximum) of the frequency band centered at ω_{nm}; $p_{nm} = \bar{p}_{nm}\cdot\hat{E}$, with $\bar{p}_{nm} = \langle u_n(\bar{r})|\bar{p}|u_m(\bar{r})\rangle$ [27]; $\bar{p} = -e\bar{r}$ is the dipole moment; ρ_{mm} and ρ_{nn} are the probability of the system being in the initial state m and the final state n, respectively.

The dielectric function, at the frequency corresponding to the bandgap between the conduction and the valence bands, of the bulk material of QD's can be expressed as

$$\epsilon_{\mathrm{QD}}(\omega) = \epsilon_b + \frac{\dfrac{2}{V_{\mathrm{QD}}}\dfrac{e^2}{m_0\epsilon_0}\xi_{\mathrm{os}}}{\omega^2 - \omega_0^2 - 2j\gamma\omega}\left[f_c(E_e) - f_v(E_h)\right] \tag{7}$$

where m_0 is the mass of a free electron, ϵ_0 the dielectric constant in free space, γ the HWHM of the frequency band centered at ω_0, ϵ_b the real part of the dielectric constant of the bulk material of the QD's, $V_{\mathrm{QD}} = (4\pi/3)a^3$ the volume of a single QD, and $N = 2/V_{\mathrm{QD}}$ [26],

$$\xi_{\mathrm{os}} = \frac{2}{m_o\hbar\omega_o}M_b^2\left|\iiint\Psi_e(\bar{r})\Psi_h(\bar{r})d\bar{r}\right|^2 \tag{8}$$

is the oscillator strength [26], with $\Psi_e(\bar{r})$ and $\Psi_h(\bar{r})$ the wave functions of electrons and holes,

respectively, and $|\iiint \Psi_e(\bar{r})\Psi_h(\bar{r})d\bar{r}| \simeq 1$; $M_b^2 = (m_0/6)E_p$, with E_p (in eV) the plasmon energy;

$$f_c(E_e) = \frac{1}{1 + e^{(E_e - E_F^{\text{bulk}})/(\kappa T)}} \tag{9}$$

$$f_v(E_h) = \frac{1}{1 + e^{(E_h - E_F^{\text{bulk}})/(\kappa T)}} \tag{10}$$

are the Fermi-Dirac distributions of electrons and holes, respectively; E_e and E_h are the energy levels of electrons and holes, respectively, in the bulk material of QD's.

Similar to (7), the dielectric functions at the frequencies corresponding to the valence-to-intermediate and intermediate-to-conduction bandgaps can be expressed as

$$\epsilon_{\text{QD},iv}(\omega) = \epsilon_b + \frac{\dfrac{2}{V_{\text{QD}}}\dfrac{e^2}{m_0\epsilon_0}\xi_{\text{os},iv}}{\omega^2 - \omega_{0,iv}^2 - 2j\gamma\omega}\left[f_{\text{ib}} - f_v\right] \tag{11}$$

$$\epsilon_{\text{QD},ci}(\omega) = \epsilon_b + \frac{\dfrac{2}{V_{\text{QD}}}\dfrac{e^2}{m_0\epsilon_0}\xi_{\text{os},ci}}{\omega^2 - \omega_{0,ci}^2 - 2j\gamma\omega}\left[f_c - f_{\text{ib}}\right] \tag{12}$$

where

$$\xi_{\text{os},iv} = \frac{2}{m_o\hbar\omega_{o,iv}} M_b^2 \left|\iiint \Psi_e(\bar{r})\Psi_h(\bar{r})d\bar{r}\right|^2$$

$$\xi_{\text{os},ci} = \frac{2}{m_o\hbar\omega_{o,ci}} M_b^2 \left|\iiint \Psi_e(\bar{r})\Psi_h(\bar{r})d\bar{r}\right|^2$$

and

$$f_{\text{ib}} = \frac{1}{1 + e^{(E_{iv} - E_{fi})/(\kappa T)}}$$

is the occupation probability in the intermediate band [10, 28];

$$E_{fi} = \frac{E_c + E_v}{2} + \frac{\kappa T}{2}\ln\frac{N_v}{N_c}$$

is the Fermi level of the matrix in the intrinsic region; E_c and E_v are the energy levels of the conduction band and the valence band, respectively, of the matrix; N_c and N_v are the number density of states of the electrons and the holes, respectively.

The absorption coefficients in the valence-to-intermediate and intermediate-to-conduction bands can thus can be derived from (11) and (12) as

$$\alpha_{iv} = 2k_0 n''_{iv}(\omega) \tag{13}$$

$$\alpha_{ci} = 2k_0 n''_{ci}(\omega) \tag{14}$$

where k_0 is the wavenumber in free space, and the complex refractive indices are derived from the dielectric functions as

$$n'_{iv} - jn''_{iv} = \sqrt{\epsilon_{\text{QD},iv}}$$

$$n'_{ci} - jn''_{ci} = \sqrt{\epsilon_{\text{QD},ci}}$$

2.3. Current Density of Solar Cells

As shown in Fig. 2, the photons with energy lower than the original bandgap can now be absorbed due to the presence of an intermediate band. Three different generation rates, associated with the

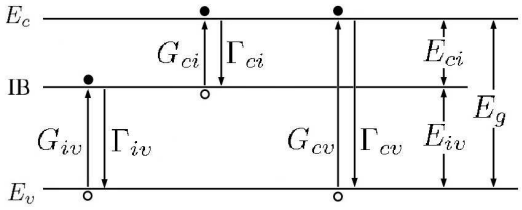

Figure 2. Band diagram with the presence of an intermediate band.

valence-band/conduction-band transition ($G_{cv}(x)$), the intermediate-band/conduction-band transition ($G_{ci}(x)$) and the valence-band/intermediate-band transition ($G_{iv}(x)$), are determined as [17]

$$G_{cv}(x) = \int_{E_g}^{\infty} \phi(E)\alpha_{cv}(E)e^{-\alpha_{cv}(E)x}dE \tag{15}$$

$$G_{ci}(x) = \gamma_f \int_{E_{ci}}^{E_{iv}} \phi(E)\alpha_{ci}(E)e^{-\alpha_{ci}(E)x}dE \tag{16}$$

$$G_{iv}(x) = \gamma_f \int_{E_{iv}}^{E_g} \phi(E)\alpha_{iv}(E)e^{-\alpha_{iv}(E)x}dE \tag{17}$$

with the accompanying bandgap energies of E_g, E_{ci} and E_{iv}, respectively; $\phi(E)$ is the spectrum of photons incident upon the top surface of the layer embedding QD's; x is the distance measured from the top surface; α_{cv}, α_{ci} and α_{iv} are the associated absorption coefficients; γ_f is the fractional volume (f_{QD}) of QD's in the matrix.

Figure 3(a) shows the arrangement of quantum dots in a regular grid as in [14, 16, 20, 29]. Typically, QD's are placed closely in the intrinsic layer so that the electron wave functions at the QD's overlap to create a continuous intermediate band [18]. It is suggested that QD's should be placed as close together as possible to increase the absorption coefficient, while not to induce the stimulated emission effect [20]. In [20], QD's with radius of 3.9 nm and spacing of $d \geq 10$ nm have been considered. Following this trend, the fractional volume of the dots will be at most 24.7%. Fig. 3(b) shows a staggered grid of QD's, which leads to a maximum fractional volume of $f_{\mathrm{QD}} = 32.3\%$.

Figure 4 shows the band diagram of a *p-i-n* solar cell, the Fermi-levels in the intrinsic layer are approximated as constant, under the assumption of infinite mobility of free carriers [29], which implies infinite diffusion lengths. Hence, the solar cell is relatively thin compared with the diffusion lengths. The QD's are embedded in the intrinsic layer ($0 < x < W_F$), in which the electron and the hole

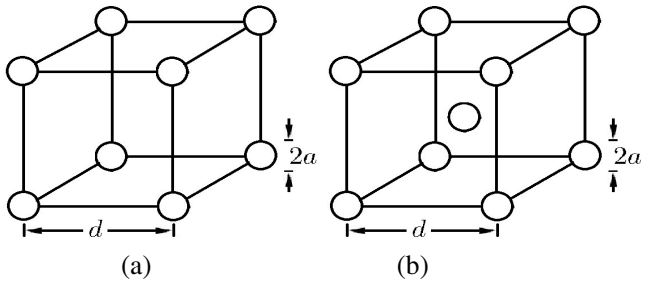

Figure 3. Quantum dots arranged in (a) a regular grid [14, 16, 20, 29] and (b) a staggered grid.

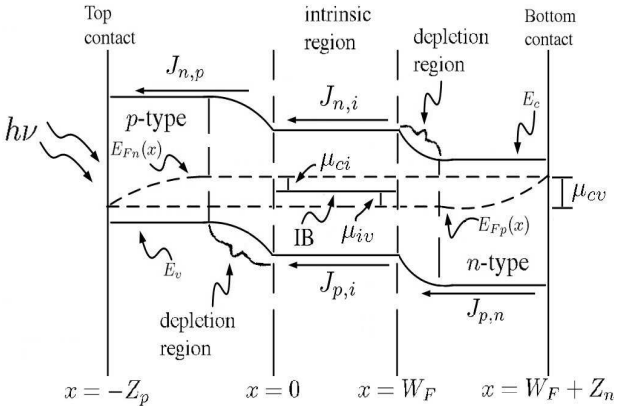

Figure 4. Band diagram of a *p-i-n* solar cell with an intermediate band.

concentrations satisfy [19]

$$D_n \frac{d^2 n}{dx^2} - \Gamma_{cv} - \Gamma_{ci} + G_{cv} + G_{ci} = 0$$

$$D_p \frac{d^2 p}{dx^2} - \Gamma_{cv} - \Gamma_{iv} + G_{cv} + G_{iv} = 0$$

where D_n and D_p are the diffusion coefficients of electrons and holes, respectively; Γ_{cv}, Γ_{ci} and Γ_{iv} are the recombination rates associated with the three different bandgaps as were mentioned.

The boundary conditions at the interface of the intrinsic layer are [19]

$$D_n \frac{dn}{dx} = \frac{1}{e} J_{n,p}, \qquad x = 0$$

$$-D_p \frac{dp}{dx} = \frac{1}{e} J_{p,n}, \qquad x = W_F$$

Thus, the hole current density at $x = 0$ can be expressed as

$$J_{p,i}(x=0) = e \int_{E_g}^{\infty} dE \phi_o \frac{\alpha_{cv} L_p}{\alpha_{cv}^2 L_p^2 - 1} \left[\frac{\alpha_{cv} L_p e^{-\alpha_{cv} W_F} + \sinh(W_F/L_p)}{\cosh(W_F/L_p)} - \alpha_{cv} L_p \right]$$

$$+\gamma_f e \int_{E_{iv}}^{E_g} dE \phi_o \left(\frac{\alpha_{iv} L_p}{\alpha_{iv}^2 L_p^2 - 1} \right) \left[\frac{\alpha_{iv} L_p e^{-\alpha_{iv} W_F} + \sinh(W_F/L_p)}{\cosh(W_F/L_p)} - \alpha_{iv} L_p \right] + \frac{J_{p,n}}{\cosh(W_F/L_p)} \quad (18)$$

where L_p is the diffusion length in the intrinsic layer.

Similarly, the electron current density at $x = W_F$ can be expressed as

$$J_{n,i}(x=W_F) = e \int_{E_g}^{\infty} dE \phi_o \frac{\alpha_{cv} L_n}{\alpha_{cv}^2 L_n^2 - 1} \left[\frac{\alpha_{cv} L_n e^{-\alpha_{cv} W_F} + \sinh(W_F/L_n)}{\cosh(W_F/L_n)} - \alpha_{cv} L_n \right]$$

$$+\gamma_f e \int_{E_{ci}}^{E_{iv}} dE \phi_o \left(\frac{\alpha_{ci} L_n}{\alpha_{ci}^2 L_n^2 - 1} \right) \left[\frac{e^{-\alpha_{ci} W_F} \sinh(W_F/L_n) - \alpha_{ci} L_n}{\cosh(W_F/L_n)} + \alpha_{ci} L_n e^{-\alpha_{ci} W_F} \right] + \frac{J_{n,p}}{\cosh(W_F/L_n)} \quad (19)$$

where L_n is the diffusion length in the intrinsic layer.

The total short-circuit current density matches at the boundaries at $x = 0$ and $x = W_F$ to indicate that there is no net current from the intermediate band to the external circuit [17]

$$J_{\rm sc} = -\left[J_{n,p}(x=0) + J_{p,i}(x=0) \right] = -\left[J_{p,n}(x=W_F) + J_{n,i}(x=W_F) \right] \quad (20)$$

where the minus sign indicates that $J_{\rm sc}$ flows in the $-x$ direction. Note that $J_{n,p}$ is the electron current generated in the p-layer, and $J_{p,n}$ is the hole current generated in the n-layer [17]. Both terms are dependent on the layer thickness and material properties [1].

Recombination process takes place in the n-type and the p-type quasi-neutral regions, the depletion region and the intrinsic region. The recombination current density in the quasi-neutral regions can be expressed as [1, 17]

$$J_{r,q} = \left[\frac{e n_i^2 D_n}{L_n N_A} \frac{(S_n L_n/D_n)\cosh(Z_p/L_n) + \sinh(Z_p/L_n)}{(S_n L_n/D_n)\sinh(Z_p/L_n) + \cosh(Z_p/L_n)} \right.$$

$$\left. + \frac{e n_i^2 D_p}{L_p N_D} \frac{(S_p L_p/D_p)\cosh(Z_n/L_p) + \sinh(Z_n/L_p)}{(S_p L_p/D_p)\sinh(Z_n/L_p) + \cosh(Z_n/L_p)} \right] \left[e^{eV/(\kappa T)} - 1 \right] \quad (21)$$

where $n_i = N_c N_v e^{-E_g^{\rm mat}/(\kappa T)}$; N_c and N_v are the effective number density of states in the conduction band and the valence band, respectively, of the matrix material; N_D and N_A are the doping concentrations in the n-type and the p-type semiconductors, respectively; V is the forward-bias voltage. For the α-type semiconductor, with $\alpha = n$, p, S_α is the surface recombination rate, D_α the diffusion constant, L_α the diffusion length, and Z_α the thickness.

The recombination current density in the intrinsic region is contributed by three recombination processes over conduction-band/valence-band, conduction-band/intermediate band and intermediate-band/valence-band, respectively. The recombination current density attributed to the conduction-band/valence band process can be expressed in the blackbody radiation model as [17]

$$J_{r,cv} = e\frac{2\pi}{h^3c^2}\left[e^{eV/(\kappa T)}-1\right]\int_{E_g}^{\infty} e^{-E/(\kappa T)}E^2\left(1-e^{-\alpha_{cv}W_F}\right)dE \tag{22}$$

where h is the Plank's constant, c is the speed of light, and $\dfrac{2\pi}{h^3c^2}\int E^2e^{-E/(\kappa T)}dE$ is the incident solar irradiance under the Plank's approximation.

By embedding QD's, additional recombination current densities, $J_{r,ci}$ over conduction-band/intermediate band and $J_{r,iv}$ over intermediate-band/valence-band, which can be expressed by modifying the blackbody radiation model in [17] with the fractional volume, γ_f, as

$$J_{r,ci} = \gamma_f e\frac{2\pi}{h^3c^2}\left[e^{e\mu_{ci}/(\kappa T)}-1\right]\int_{E_{ci}}^{E_{iv}} e^{-E/(\kappa T)}E^2\left(1-e^{-\alpha_{ci}W_F}\right)dE \tag{23}$$

$$J_{r,iv} = \gamma_f e\frac{2\pi}{h^3c^2}\left[e^{e\mu_{iv}/(\kappa T)}-1\right]\int_{E_{iv}}^{E_g} e^{-E/(\kappa T)}E^2\left(1-e^{-\alpha_{iv}W_F}\right)dE \tag{24}$$

where, as shown in Fig. 4, $\mu_{cv} = V$ is the split of Fermi levels between the n-region and the p-region; $\mu_{iv} = \zeta V$ is the split of Fermi levels between the i-region and the p-region; $\mu_{ci} = (1-\zeta)V$ is the split of Fermi levels between the i-region and the n-region; with $0 < \zeta < 1$ and $\mu_{ci} + \mu_{iv} = \mu_{cv}$ [17, 19]. In order to maintain charge neutrality in the intrisic region, it is required that $J_{r,ci} = J_{r,iv}$ [17, 19], from which ζ is determined.

The recombination current density in the depletion region can be expressed as [17]

$$J_{r,d} = \frac{en_iW}{\tau}\left[e^{eV/(\kappa T)}-1\right] \tag{25}$$

where W is the thickness of the depletion region. In the presence of QD's, the total recombination current is derived from (21), (22), (23) and (25) as

$$J_r = J_{r,q} + J_{r,cv} + J_{r,ci} + J_{r,d} \tag{26}$$

From (20) and (26), the total current density is

$$J = J_{sc} - J_r \tag{27}$$

3. SIMULATION RESULTS AND DISCUSSIONS

When QD's are embedded in a matrix, as shown in Fig. 1, a bandgap of E_g^{QD} is created. Photons with energy equal to or higher than $E_{iv} = E_g^{\mathrm{QD}}$ can be absorbed to pumped an electron from the original valence band. Thus, an intermediate band at E_{iv} above the original valence band is created, as shown in Fig. 2. Once the desired E_{iv} is specified, the required bangap shift, $\Delta E_g = E_g^{\mathrm{QD}} - E_g^{\mathrm{bulk}}$, defined in (4) and (5), can be achieved by adjusting a with (1).

Figure 5 shows the absorption coefficient of GaAs, a typical matrix material for solar cells. The bandgap of GaAs is 1.42 eV, corresponding to a cutoff wavelength of 873 nm. A single-junction GaAs solar cell, produced by Alta Devices, is measured to achieve an efficiency of $\eta = 28.8\%$, under the AM1.5 spectrum at 298 K [5].

Figure 6(a) shows the simulated J-V curve of a single-junction GaAs p-n solar cell. The thicknesses of the p and n regions are 0.15 µm and 6.5 µm, respectively. The doping concentrations are $8\times10^{16}\,\mathrm{cm}^{-3}$ in the p region and $8\times10^{16}\,\mathrm{cm}^{-3}$ in the n region. The surface recombination rate at the top and the bottom contacts is set to zero. The short-circuit current density is $J_{\mathrm{sc}} = 31.9\,\mathrm{mA/cm}^2$, the open-circuit voltage is $V_{\mathrm{oc}} = 1.05\,\mathrm{V}$, $FF = 0.85$, and the efficiency is $\eta = 28.58\%$, comparable to that in [5].

Figure 6(b) shows the external quantum efficiency (EQE) of this solar cell, defined as

$$\mathrm{EQE} = \frac{J_{\mathrm{sc}}}{e\phi_{io}} \tag{28}$$

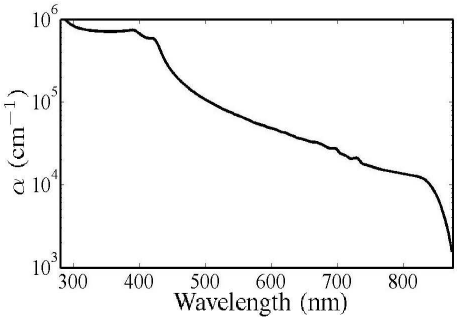

Figure 5. Absorption coefficient of GaAs [30].

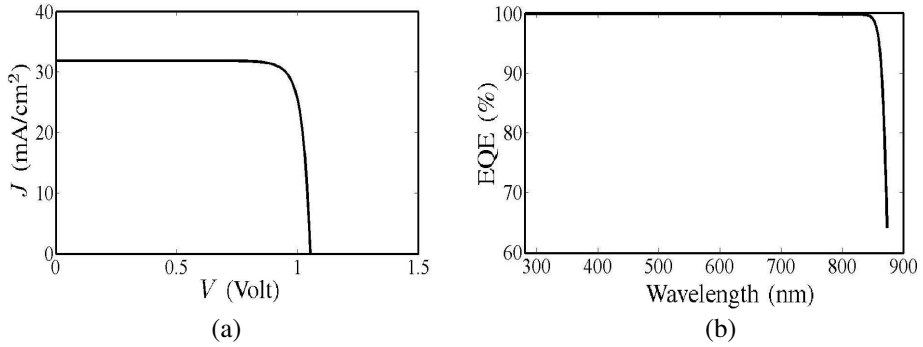

Figure 6. (a) J-V curve and (b) EQE of a single-junction GaAs p-n solar cell, with $\eta = 28.58\%$.

where ϕ_{io} is the incident photon flux on the top surface of the cell. The EQE is the generation rate ($1/\text{cm}^2/\text{s}$) of net free carriers per incident photon. It depends on the doping concentrations, layer thickness and material properties, including the absorption coefficient, the diffusivity of free carriers, and the surface recombination rate on the top and bottom interfaces. The surface recombination rates on the top and bottom interfaces are approximated as zero. The EQE is low at long wavelengths, mainly due to the low absorption coefficient.

To enhance the efficiency, an intrinsic layer is inserted to make a single-junction GaAs p-i-n solar cell. Fig. 7(a) shows its η and J_{sc} at different doping concentrations, with $N_A = N_D$. The thicknesses of the p, i and n regions are 0.8, 2.8 and 3 μm, respectively. The surface recombination rate at the top and bottom contacts is set to zero. At lower doping concentrations, the lifetime of minority carriers is increased due to lower possibility of recombination, hence higher η and J_{sc} are achieved.

In Fig. 7(b), the built-in potential becomes lower than the open-circuit voltage, V_{oc}, when the doping concentration is too small, which is nonphysical. Hence, a higher doping concentration is preferred. The EQE shown in Fig. 7(c) is nearly a constant at lower wavelengths.

Figures 8, 9, 10 show how the thicknesses of the i, p and n regions, respectively, affect the efficiency, J_{sc}, V_{oc} and EQE's of the p-i-n solar cell. The reference doping concentrations are $N_A = 8 \times 10^{16}\,\text{cm}^{-3}$ and $N_D = 2.5 \times 10^{15}\,\text{cm}^{-3}$. The surface recombination rate at the top and the bottom contacts is set to zero.

As shown in Figs. 8(a) and 8(b), the efficiency, J_{sc} and V_{oc} increase with increasing W_F. As W_F increases, the recombination process becomes stronger than the generation process. Hence, the efficiency appears to saturate when $W_F \geq 3.5\,\mu\text{m}$.

In the intrinsic region, the carrier lifetime is relatively long due to its low doping concentration. Hence, a larger W_F leads to a higher EQE, as shown in Fig. 8(c).

Figures 9(a) and 10(a) show that the efficiency increases as Z_p or Z_n decreases. Figs. 9(b) and 10(b) show that V_{oc} increases while J_{sc} decreases as Z_p or Z_n decreases. When Z_p or Z_n gets smaller, less space is left for the generation process to take effect, hence J_{sc} decreases. In addition, when Z_p or Z_n becomes shorter than the diffusion length of the minority carriers, the recombination process

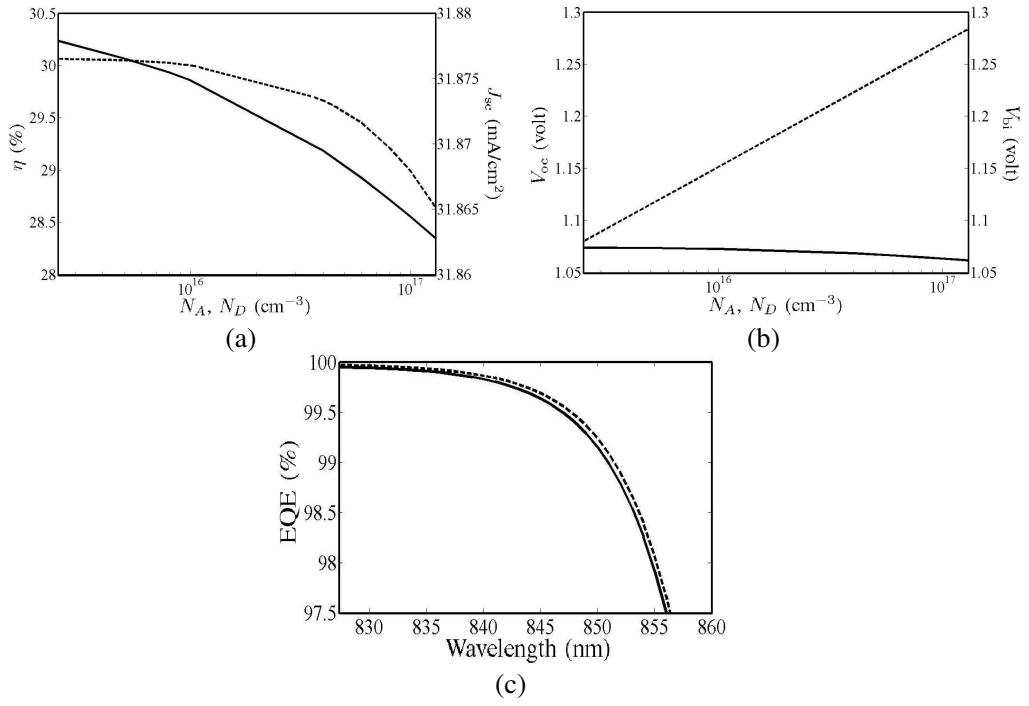

Figure 7. (a) η (——), $J_{\rm sc}$ ($-\,-\,-$) and (b) $V_{\rm oc}$ (——), $V_{\rm bi}$ ($-\,-\,-$) of a single-junction GaAs p-i-n solar cell, at different doping concentrations ($N_A = N_D$). (c) EQE at $N_A = N_D = 8 \times 10^{16}$ (cm^{-3}) (——) and $N_A = N_D = 2.5 \times 10^{15}$ (cm^{-3}) ($-\,-\,-$). The thicknesses of p, i and n regions are 0.8, 2.8 and 3 µm, respectively.

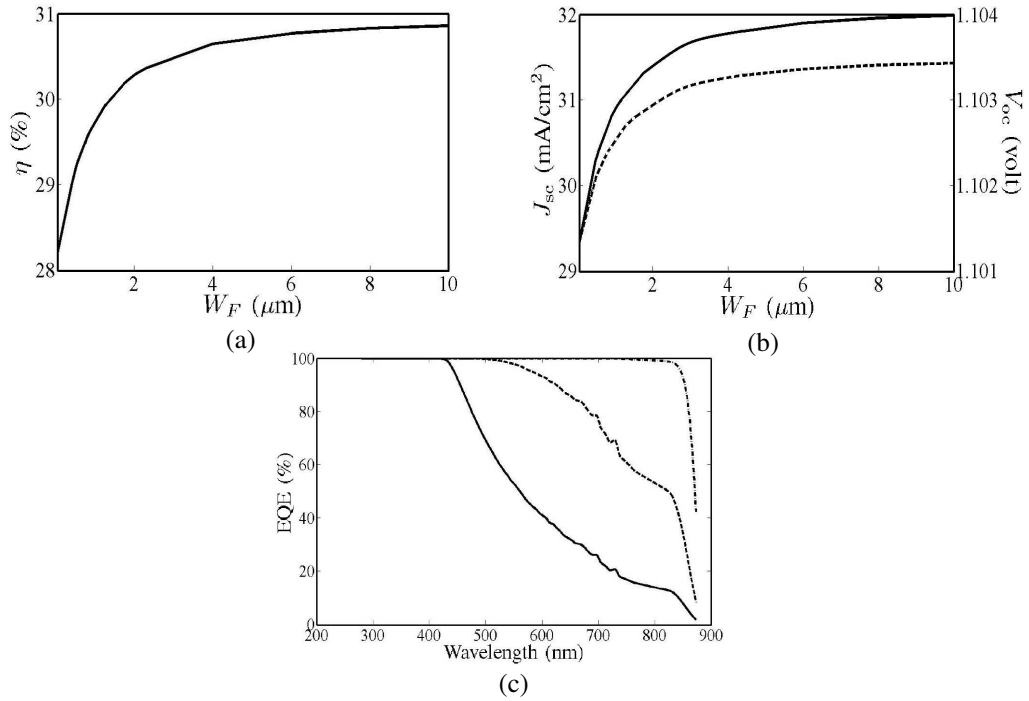

Figure 8. (a) η, (b) $J_{\rm sc}$ (——) and $V_{\rm oc}$ ($-\,-\,-$), and (c) EQE of the solar cell with different W_F's; ——: $W_F = 0.05$ µm, $-\,-\,-$: $W_F = 0.5$ µm, $-.-$: $W_F = 3.5$ µm. The thicknesses of p and n regions are 0.04 and 1.12 µm, respectively; the doping concentrations are $N_A = 8 \times 10^{16}\,{\rm cm}^{-3}$, $N_D = 2.5 \times 10^{15}\,{\rm cm}^{-3}$.

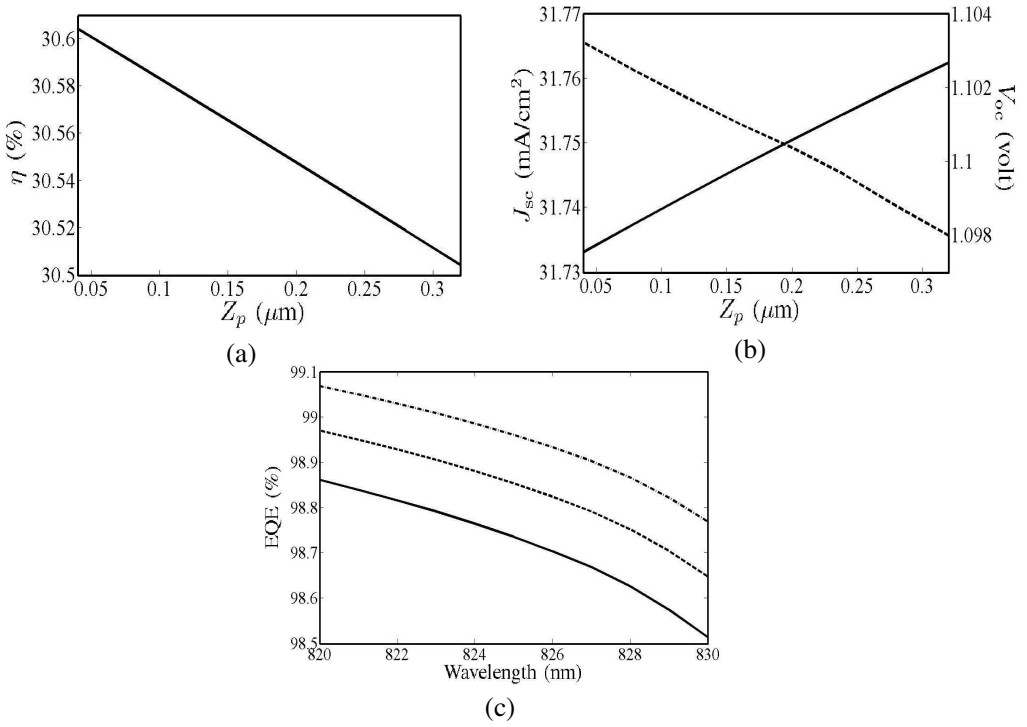

Figure 9. (a) η, (b) $J_{\rm sc}$ (——) and $V_{\rm oc}$ (− − −), and (c) EQE of the solar cell with different Z_p's; ——: $Z_p = 0.04\,\mu$m, − − −: $Z_p = 0.12\,\mu$m, −.−: $Z_p = 0.2\,\mu$m. The thicknesses of i and n regions are 3.5 and 1.12 μm, respectively; the doping concentrations are $N_A = 8 \times 10^{16}\,{\rm cm}^{-3}$, $N_D = 2.5 \times 10^{15}\,{\rm cm}^{-3}$.

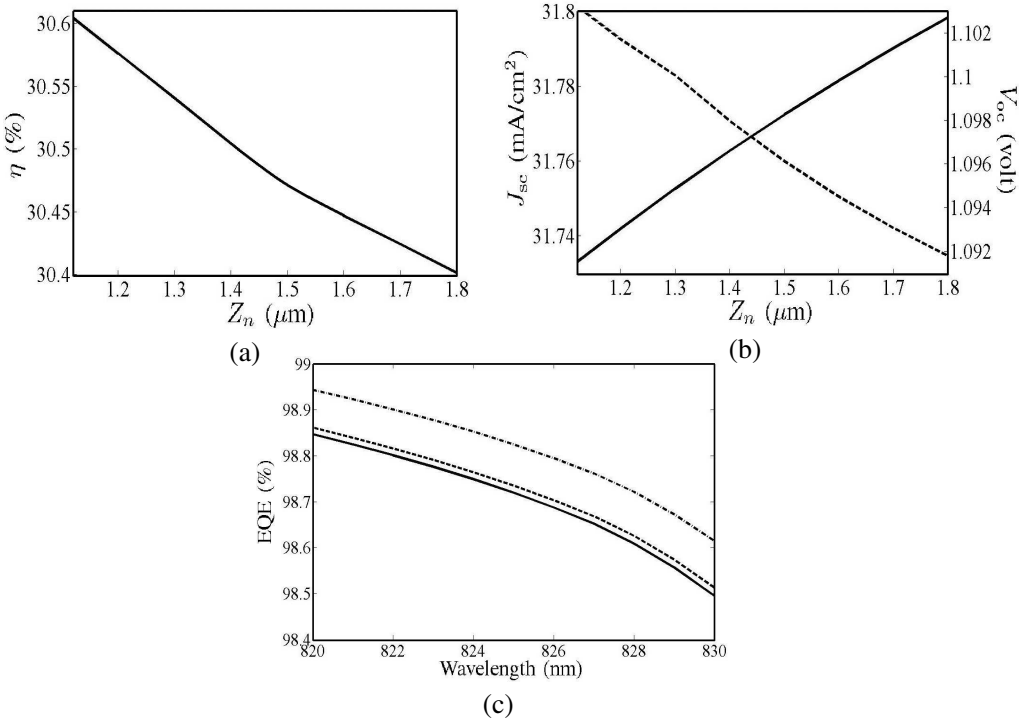

Figure 10. (a) η, (b) $J_{\rm sc}$ (——) and $V_{\rm oc}$ (− − −), and (c) EQE of the solar cell with different Z_n's; ——: $Z_n = 1.12\,\mu$m, − − −: $Z_n = 1.20\,\mu$m, −.−: $Z_n = 1.40\,\mu$m. The thicknesses of p and i regions are 0.04 and 3.5 μm, respectively; the doping concentrations are $N_A = 8 \times 10^{16}\,{\rm cm}^{-3}$, $N_D = 2.5 \times 10^{15}\,{\rm cm}^{-3}$.

becomes weaker, leading to lower $J_{r,q}$ and J_r. If $J_{\rm sc}$ does not decrease as much as J_r when Z_p or Z_n is decreased, $V_{\rm oc}$ will increase.

Figures 9(c) and 10(c) show that the EQE is lower at smaller Z_p or Z_n. As a comparison, Figs. 9(a) and 10(a) show that the efficiency is higher at smaller Z_p or Z_n. Note that the definition of EQE in (28) involves only $J_{\rm sc}$, which is related to the generation process; the recombination current is not considered.

In order to achieve high efficiency, smaller Z_p and Z_n are chosen, leading to a higher $V_{\rm oc}$, which in turn demands a higher $V_{\rm bi}$. Therefore, a larger number of $N_A \times N_D$ is required.

As shown in Fig. 7(c), the EQE at shorter wavelengths is insensitive to the doping concentrations. Since the high-energy photons are mainly absorbed in the p region, a higher N_A is preferred. Hence, we choose $N_A = 8 \times 10^{16}\,{\rm cm}^{-3}$ and $N_D = 2.5 \times 10^{15}\,{\rm cm}^{-3}$. The thicknesses of the p, i and n regions are 0.04 µm, 3.5 µm and 1.12 µm, respectively. The surface recombination rate at the top and the bottom contacts is set to zero. As shown in Fig. 11, we achieve $J_{\rm sc} = 31.7\,{\rm mA/cm}^2$, $V_{\rm oc} = 1.103\,{\rm V}$, FF $= 0.87$, and $\eta = 30.60\%$.

Embedding the QD's in the intrinsic layer of the cell, higher $f_{\rm QD}$ means higher density of the intermediate band, which leads to a higher rate of free-carrier generation. Thus, we take the arrangement of QD's as in Fig. 3(b), with $f_{\rm QD} = 32.3\%$. Fig. 12 shows the bandgap of an InAs QD in the GaAs matrix, calculated using the method described in Section 2.1. The required radius of QD's thus can be obtained.

To ensure the intermediate band is half filled, it is required that $f_{\rm ib} = 0.5$ in (11) and (12). Also, to make sure no net current is contributed by the intermediate band, (20) and $J_{r,ci} = J_{r,iv}$ are imposed. Under these restrictions, the highest η of 31.65% is achieved with $E_{iv} = 0.94\,{\rm eV}$ and $a = 1.19\,{\rm nm}$.

Figure 13 shows the simulated J-V curve of a single-junction GaAs p-i-n solar cell, embedded with InAs QD's at a fractional volume of 32.3%, $N_A = 8 \times 10^{16}\,{\rm cm}^{-3}$, $N_D = 2.5 \times 10^{15}\,{\rm cm}^{-3}$; the thicknesses of p, i and n regions are 0.3, 1.3 and 1.6 µm, respectively. We obtain $J_{\rm sc} = 34.87\,{\rm mA/cm}^2$,

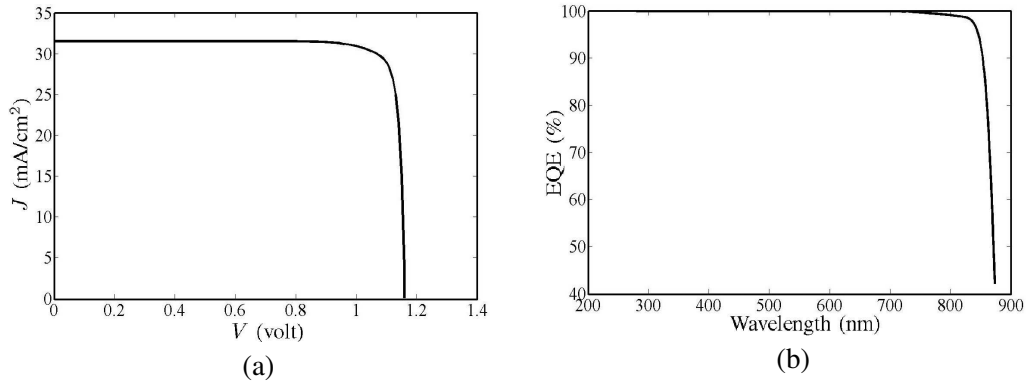

Figure 11. (a) J-V curve and (b) EQE of a single-junction GaAs p-i-n solar cell. $N_A = 8 \times 10^{16}\,{\rm cm}^{-3}$, $N_D = 2.5 \times 10^{15}\,{\rm cm}^{-3}$; the thicknesses of p, i and n regions are 0.04 µm, 3.5 µm and 1.12 µm, respectively; $J_{\rm sc} = 31.7\,{\rm mA/cm}^2$, $V_{\rm oc} = 1.103\,{\rm V}$, $\eta = 30.60\%$.

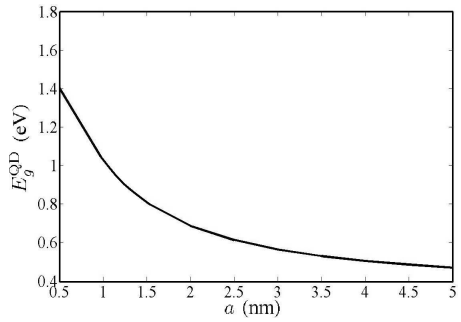

Figure 12. Bandgap of an InAs QD in the GaAs matrix.

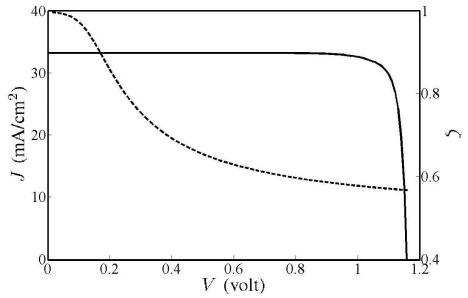

Figure 13. J-V curve (– – –) and ζ (——-) of a single-junction GaAs p-i-n solar cell with InAs QD's; $f_{\rm QD} = 32.3\%$, $N_A = 8 \times 10^{16}\,{\rm cm}^{-3}$, $N_D = 2.5 \times 10^{15}\,{\rm cm}^{-3}$; the thicknesses of p, i and n regions are 0.3, 1.3 and 1.6 μm, respectively; $J_{\rm sc} = 34.87\,{\rm mA/cm}^2$, $V_{\rm oc} = 1.075\,{\rm V}$, $\eta = 31.65\%$.

$V_{\rm oc} = 1.075\,{\rm V}$, and $\eta = 31.65\%$. Note that the thicknesses of p, i and n regions are not the same as those adopted to achieve the highest η, as shown in Fig. 11, of the p-i-n cell without QD's. With the presence an intermediate band between the original valence and conduction bands, the generation and recombination mechanisms are modified. The additional condition on current density matching at $x = 0$ and $x = W_F$ also affect the optimum choice of layer thicknesses.

Figure 13 also shows the ratio, $\zeta = \mu_{iv}/V$, at different forward-bias voltages, with $J_{r,ci}$ and $J_{r,iv}$ calculated using (23) and (24), respectively. As V increases, the built-in voltage shown in Fig. 4 decreases, leading to a larger split between the quasi-fermi levels, E_{fn} and E_{fp}, as well as larger μ_{iv}. Since μ_{iv} increases slower than V, ζ becomes smaller at higher V.

Figure 14 shows the absorption coefficients at different wavelengths, where the intermediate band is designed at 0.94 eV above the valence band, namely, $E_{iv} = 0.94\,{\rm eV}$ and $E_{ci} = 0.48\,{\rm eV}$. The absorption coefficients in the valence-band/intermediate-band and the intermediate-band/conduction-band transitions are derived from (13) and (14), with $\hbar\gamma = 1.5\,{\rm meV}$ [26]. The absorption coefficient in the valence-band/conduction-band transition is that of the matrix.

Figure 15 shows the EQE of the solar cell with and without QD's, respectively. In the absence of QD's, the bandgap is $E_g^{\rm mat} = 1.42\,{\rm eV}$, corresponding to 873 nm in wavelength. The EQE at the wavelength above 873 nm is zero because no free carriers can be generated.

When QD's are embedded, besides the photons with energy higher than $E_g^{\rm mat}$, some photons with energy lower than $E_g^{\rm mat}$ can now be absorbed. Free carriers can be generated by photons with energy ranging from $E_{ci} = 0.48\,{\rm ev}$ to $E_g^{\rm mat} = 1.42\,{\rm eV}$, corresponding to wavelengths from 873 to 2583 nm. The additional absorption in this spectral region is due to the existence of the intermediate band. However, note that the EQE in Fig. 15, the EQE is only presented to $E_{iv} = 0.94\,{\rm eV}$, corresponding to 1319 nm in wavelength. Because the electrons must be excited simultaneously from valence to intermediate band and from intermediate to conduction band to generate current in the intrinsic region. Hence, the EQE is calculated with photon energy above the higher of E_{iv} and E_{ci}.

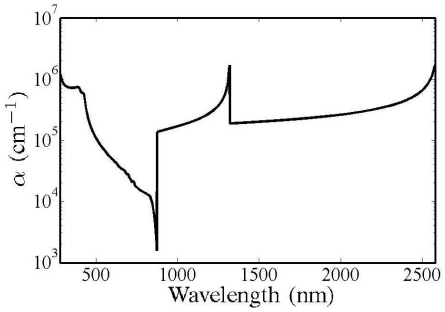

Figure 14. Absorption coefficients as a function of wavelengths.

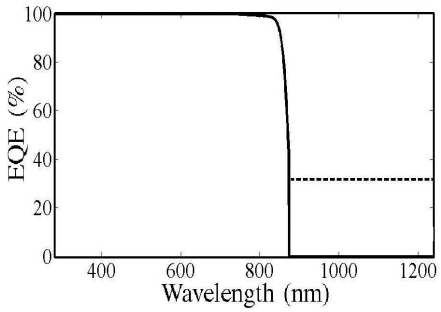

Figure 15. EQE of GaAs p-i-n solar cell without (——) and with (– – –) QD's, $f_{\rm QD} = 32.3\%$, other parameters are the same as in Fig. 13.

The EQE at short wavelengths and long wavelengths (close to the cutoff wavelength) are dominate by the surface recombination on the top and the bottom contact, respectively, of the solar cell. That of the intermediate wavelengths is dominate by the bulk recombination loss in the solar cell. The embedded QD's can enhance the absorption at long wavelengths, thus compensating for the loss on the bottom contact. Hence, higher EQE can be reached at long wavelengths. In this work, the surface recombination at the top contact is approximated as zero, which can be achieved by design. Hence, the EQE at short wavelengths can also be improved.

4. CONCLUSIONS

The efficiency of a single-junction *p-i-n* solar cell has been increased by embedding quantum dots in the intrinsic layer. With the embedded QD's, an intermediate band is created between the valence and the conduction bands to absorb additional solar irradiance carried by photons with energy lower than the original bandgap. The energy level of the intermediate band depends on the size and material properties of the quantum dots, which can be tuned to achieve the highest absorptance. To ensure the efficiency enhancement by embedding QD's, a more packed arrangement of quantum dots has been proposed to increase their fractional volume in the intrinsic region. An efficiency of $\eta = 31.65\%$ has been achieved, with $E_{iv} = 0.94\,\text{eV}$ and the radius of InAs QD's being $a = 1.19\,\text{nm}$. A conventional GaAs single-junction *p-i-n* solar cell has also been fine-tuned for reference, which has an optimal efficiency of $\eta = 30.60\%$. An efficiency improvement of 1.05% is thus achieved by embedding InAs quantum dots.

ACKNOWLEDGMENT

This work was sponsored by the National Science Council, Taiwan, ROC, under contract NSC 101-2221-E-002-129.

REFERENCES

1. Fonash, S. J., *Solar Cell Device Physics*, 2nd Edition, Academic Press, 2010.
2. Shockley, W. and H. J. Queisser, "Detailed balance limit of efficiency of *pn* junction solar cells," *J. Appl. Phys.*, Vol. 3, No. 3, 510–519, 1961.
3. Landsberg, P. T. and P. Baruch, "The thermodynamics of the conversion of radiation energy for photovoltaics," *J. Phys. A: Math.*, Vol. 22, 1911–1926, 1989.
4. Solankia, C. S. and G. Beaucarneb, "Advanced solar cell concepts," *Energy Sustain. Develop.*, Vol. 11, No. 3, 17–23, 2007.
5. Kayes, B. M., et al., "27.6% conversion efficiency, a new record for single-junction solar cells under 1 sun illumination," *Photovolt. Special. Conf.*, 4–8, 2011.
6. Green, M. A., et al., "Solar cell efficiency tables (version 42)," *Prog. Photovolt. Res. Appl.*, Vol. 21, No. 5, 827–837, 2013.
7. Green, M. A., "Third generation photovoltaics: Ultra-high conversion efficiency at low cost," *Prog. Photovolt. Res. Appl.*, Vol. 9, 123–135, 2001.
8. Newman, F., et al., "Optimization of inverted metamorphic multijunction solar cells for field-deployed concentrating PV systems," *IEEE Photovolt. Special. Conf.*, 1611–1616, 2009.
9. Luque, A. and S. Hegedus, *Handbook of Photovoltaic Science and Engineering*, 93–107, John Wiley, 2003.
10. Hu, W. G., T. Inoue, O. Kojima, and T. Kita, "Effects of absorption coefficients and intermediate-band filling in InAs/GaAs quantum dot solar cells," *Applied Phys. Lett.*, Vol. 97, 193106, 2010.
11. Luque, A., A. Marti, and C. Stanley, "Understanding intermediate-band solar cells," *Nature Photon.*, Vol. 6, 146–152, 2012.
12. Nakata, Y., Y. Sugiyama, and M. Sugawara, *Molecular Beam Epitaxy Growth of Self-assembled InAs/GaAs Quantum Dots*, Ch. 2, Academic, 1990.

13. Bhattacharya, P., S. Ghosh, and A. D. Stiff-Roberts, "Quantum dot opto-electronic devices," *Ann. Rev. Materials Res.*, Vol. 34, 1–40, 2004.
14. Cuadra, L., A. Marti, and A. Luque, "Present status of intermediate band solar cell research," *Thin Solid Films,*, Vols. 451–452, 593–599, 2004.
15. Raffaelle, R. P., et al., "Multi-junction solar cell spectral tuning with quantum dots," *IEEE World Conf. Photovolt. Energy Conv.*, Vol. 1, 162–166, 2006.
16. Gorji, N. E., M. H. Zandic, M. Houshmandc, and M. Shokri, "Transition and recombination rates in intermediate band solar cells," *Scientia Iranica*, Vol. 19, No. 3, 806–811, 2012.
17. Lin, C. C., M. H. Tan, C. P. Tsai, K. Y. Chuang, and T. S. Lay, "Numerical study of quantum-dot-embedded solar cells," *IEEE J. Select. Topics Quantum Electron.*, Vol. 19, No. 5, 1–10, 2013.
18. Marti, A., L. Cuadra, and A. Luque, "Quantum dot intermediate band solar cell," *IEEE Photovolt. Special. Conf.*, 940–943, 2000.
19. Lin, A. S., "Modeling of solar cell efficiency improvement using optical gratings and intermediate absorption band," Ph.D. Thesis, University of Michigan, 2010.
20. Marti, A., L. Cuadra, and A. Luque, "Design constraints of the quantum-dot intermediate band solar cell," *Physica E*, Vol. 14, Nos. 1–2, 150–157, 2002.
21. Pellegrini, G., G. Mattei, and P. Mazzoldi, "Finite depth square well model: Applicability and limitations," *J. Appl. Phys.*, Vol. 97, No. 7, 193106, 2005.
22. Horiguchi, S., "Validity of effective mass theory for energy levels in Si quantum wires," *Physica B*, Vol. 227, Nos. 1–4, 336–338, 1996.
23. Nanda, K. K., F. E. Kruis, and H. Fissan, "Energy levels in embedded semiconductor nanoparticles and nanowires," *Nano Lett.*, Vol. 1, No. 11, 605–611, 2011.
24. Baskoutas, S. and A. F. Terzis, "Size-dependent band gap of colloidal quantum dots," *J. Appl. Phys.*, Vol. 99, No. 1, 013708, 2006.
25. Kasap, S. and P. Capper, *Handbook of Electronic and Photonic Materials*, 54–327, Springer, 2006.
26. Holmstrom, P., L. Thylen, and A. Bratkovsky, "Dielectric function of quantum dots in the strong confinement regime," *J. Appl. Phys.*, Vol. 107, No. 6, 064307, 2010.
27. Boyd, R., *Nonlinear Optics*, 135–206, Elsevier, 2008.
28. Luque, A., A. Marti, N. Lopez, E. Antolin, E. Canovas, C. Stanley, C. Farmer, and P. Diaz, "Operation of the intermediate band solar cell under nonideal space charge region conditions and half filling of the intermediate band," *J. Appl. Phys.*, Vol. 99, 094503, 2006.
29. Marti, A., L. Cuadra, and A. Luque, "Partial filling of a quantum dot intermediate band for solar cells," *IEEE Trans. Electron. Dev.*, Vol. 48, No. 10, 2394–2399, 2002.
30. Palik, E. D., *Handbook of Optical Constants of Solids*, Academic Press, 1998.